



Air-breathing direct formic acid microfluidic fuel cell with an array of cylinder anodes



Xun Zhu ^{a, b, *}, Biao Zhang ^{a, b}, Ding-Ding Ye ^{a, b}, Jun Li ^{a, b}, Qiang Liao ^{a, b}

^a Key Laboratory of Low-grade Energy Utilization Technologies and Systems, Chongqing University, Chongqing 400030, China

^b Institute of Engineering Thermophysics, Chongqing University, Chongqing 400030, China

HIGHLIGHTS

- We proposed an air-breathing microfluidic fuel cell with an array of cylinder anodes.
- The absence of 2 spacers near the cathode enhances proton transfer and performance.
- The dynamic behavior of CO₂ bubbles was studied by visualization.
- CO₂ bubbles were confined within the anodes array and removed periodically.
- A maximum single pass fuel utilization rate of 87.6% was obtained.

ARTICLE INFO

Article history:

Received 29 June 2013

Received in revised form

23 August 2013

Accepted 26 August 2013

Available online 5 September 2013

Keywords:

Microfluidic fuel cell
Membraneless fuel cell
Air-breathing cathode
Cylinder anode
Carbon dioxide bubble
Reactant transfer

ABSTRACT

An air-breathing direct formic acid membraneless microfluidic fuel cell using graphite cylinder arrays as the anode is proposed. The three dimensional anode volumetrically extends the reactive surface area and improves fuel utilization. The effects of spacer configuration, fuel and electrolyte concentration as well as reactant flow rate on the species transport and cell performance are investigated. The dynamic behavior of generated CO₂ bubbles is visualized and its effect on current generation is discussed. The results show that the absence of two spacers adjacent to the cathode surface improves the cell performance by reducing the proton transfer resistance. The CO₂ gas bubbles are constrained within the anode array and expelled by the fluid flow periodically. Proper reactant concentration and flow rate are crucial for cell operation. At optimum conditions, a maximum current density of 118.3 mA cm⁻² and a peak power density of 21.5 mW cm⁻² are obtained. In addition, benefit from the volumetrically stacked anodes and enhanced fuel transfer, the maximum single pass fuel utilization rate reaches up to 87.6% at the flow rate of 1 mL h⁻¹.

© 2013 Elsevier B.V. All rights reserved.

1. Introduction

Recently, rapid-developing portable electronic devices have spurred the demand for high efficient and reliable microfuel cells. Among many approaches, membraneless microfluidic fuel cell (MMFC) has been regarded as one of the most promising miniaturized power sources due to its simple architecture, high energy density, ease of system integration and elimination of membrane-related problems [1,2]. Specifically, the air-breathing MMFC shows great promise for high efficiency applications as it eliminates

the transfer limitation of dissolved oxygen and the fuel/oxidant interdiffusion for potential fuel recycle [3–8].

However, this technology is still facing many challenges, including the limitation of cell performance due to fuel transfer through the depletion boundary layer [9–11]. During the MMFC operation, both the consumption of electrode reactions and the insufficient diffusive mass transfer contribute to the formation of depletion boundary layer, which results in large fuel transfer resistance and therefore lower the cell performance [7,9,10]. Based on these results, several strategies have been proposed to enhance the fuel supply in MMFCs.

One of the strategies is to manipulate the fluid flow condition. Simply, operating at higher flow rates [12–14] (i.e., higher Peclet numbers ($Pe = UH/D$)) can replenish the depletion boundary layer more rapidly and induce a steeper concentration gradient. However, due to the short residence time, a large fraction of fuel would

* Corresponding author. Key Laboratory of Low-grade Energy Utilization Technologies and Systems, Chongqing University, Chongqing 400030, China. Tel./fax: +86 23 6510 2474.

E-mail address: zhuxun@cqu.edu.cn (X. Zhu).

pass through the fuel cell without involving in the electrochemical reactions, leading to low energy conversion efficiency. Furthermore, higher flow rates also cause flow instabilities that induce undesired fuel/oxidant crossover [12,15]. Alternatively, the fuel stream can be hydrodynamically focused to a thin layer over the anode by adjusting the flow rate ratio [9] or inserting the third stream [16]. Besides, the depletion boundary layer can also be convectively replenished via a multi-inlet/outlet configuration [10] or by creating separate spiraling flow in the fuel/oxidant streams [10,17]. However, these strategies complicate the fluidic design [6] and may increase the parasitic current [18].

Previous studies also reveal that fuel transfer highly depends on the electrode architecture. The flow through configuration with porous electrodes is the most studied architecture [6,19–23], primarily due to its increased electrode utilization and enhanced convective/diffusive transport. However, the increased pressure drop [19] and the difficulty of depositing catalyst into the micropores are still challenging. Recently, Kjeang et al. proposed a novel three-dimensional MMFC based on an array of cylinder graphite rod electrodes [24]. Because of the extended reactive area, enhanced mass transfer and the inherent advantage of non-planar liquid–electrode interface (i.e., providing high volumetric power density) [25], a better performance and higher fuel utilization rate were obtained. However, its energy conversion efficiency is intrinsically limited by the species interdiffusion. Furthermore, the vanadium redox species used in his study may reduce the cell flexibility due to the environmental concerns and should be replaced by environmental-friendly fuels. Recently, it has been demonstrated that highly active catalyst layer can be easily deposited onto the graphite rod by electrodeposition [26]. Consequently, this promising three-dimensional electrodes configuration can also be integrated to air-breathing MMFCs using common biofuels (e.g., formic acid and methanol).

During the MMFC operation, CO₂ bubbles are released as products. It has been elucidated that the gas bubbles (carbon dioxide [3,12,27], oxygen [27–31] and hydrogen [17]) would perturb the co-laminar flow interface and therefore induce unfavorable fuel crossover. This problem would become more serious in a high performance MMFC since a large amount of gas bubbles are generated at high current densities. Therefore, to develop high performance and reliable MMFCs, the bubbles must be constrained in a limited space to avoid disturbing the liquid–liquid interface. On the other hand, the constrained bubbles must be effectively removed to prevent the blockage of the electrode surface area, which in turn decreases the cell performance by hindering the fuel supply.

To enhance fuel transfer and handle the bubble distribution, an air-breathing direct formic acid MMFC using graphite cylinder arrays as the anode was developed in this study (see Fig. 1). The effects of spacer configuration, fuel and electrolyte concentration as well as reactant flow rate on the species transport and cell performance were investigated. Furthermore, the dynamic behavior of CO₂ bubbles and its effect on the chronoamperometry curve were also studied.

2. Experimental

2.1. Fuel cell construction

Fig. 1 illustrates the proposed air-breathing MMFC made from Polymethyl methacrylate (PMMA) plates. The fuel cell comprised a rectangular flow channel with the dimension of $2.5 \times 6.3 \times 40$ mm. To deliver the fuel and electrolyte, two grooves with the cross section of 1×1.5 mm were milled perpendicular to the flow channel. Two polythene tubes with an inner diameter of 1.5 mm were glued to the groove inlets. Opposite to the two grooves, a slit

outlet was fabricated at the channel end, therefore driving the fuel stream to flow through the anode array. An array of holes was drilled on the front/back plates in a hexagonal pattern with the spacing of 400 μ m. The 0.5 mm diameter anodes and spacers were fitted into the flow channel through the holes and sealed by epoxy resin. In this study, 12 cylinder anodes were prepared by electrodeposition as Zhang et al. [26] and electrically connected in parallel with the surface area of 7.5 cm². The Pd catalyst and Nafion loading were about 5 and 0.3 mg cm⁻², respectively. The air-breathing cathode was fabricated as Li et al. [32] with the Pt black (HiSPEC 1000, Alfa Aesar) loading around 3.0 mg cm⁻² and the Nafion loading about 1.0 mg cm⁻². The L-shaped cathode (see Fig. 1b) was positioned on the flow channel with Pt catalyst at the electrolyte side, having an effective surface area about 0.9 cm². A thin PMMA cover plate with a 2.5×40 mm slot was used to hold the cathode and allow the air diffusion. Two copper wires were attached to the anodes and cathode using conductive epoxy (Circuit Works CW2400, Chemtronics, USA). Between the anodes and cathode, 8 or 6 electrical-isolated spacers were used for stabilizing the fluids flow in the interdiffusion zone. The fuel cell was fastened by four bolts (not shown) and no leakage was confirmed.

2.2. Fuel cell characterization

In this study, the fuel cell was positioned horizontally with the air-breathing cathode on the top. Formic acid was used as the fuel and sulfuric acid as the electrolyte. To facilitate the proton transfer, H₂SO₄ with the same concentration to the electrolyte was added to the fuel as the supporting electrolyte. Solutions were de-aerated with high purity nitrogen for 30 min prior to experiments and driven by a dual-syringe pump (SN–50F6, Sino Medical-Device Technology Co., Ltd., China). Unless mentioned otherwise, the volumetric flow rates of the two streams were identical and specified by the operating condition. The waste solution was collected and treated for discharge.

To visualize the co-laminar flow and the dynamic behavior of CO₂ bubbles, images were recorded by a digital camera (D80, Nikon, Japan) with a macro lens through the transparent channel wall. For co-laminar flow visualization, red dyed and dye-free deionized water were used as the anolyte and the electrolyte, respectively. During the two-phase flow study, the fuel cell was operated in the potentiostatic mode at a cell voltage of 0.3 V.

The cell performance was evaluated with an electrochemical workstation (Zahner Zennium, Germany) at room temperature. The polarization curves were obtained by chronoamperometry under stepwise potentiostatic control from open circuit voltage (OCV) to 0.0 V at -0.1 V per step. The corresponding currents were recorded for 3 min. The current densities reported here were normalized to the flow channel volume (0.63 cm³, including the anodes and spacers) and were time-averaged [27]. An Ag/AgCl reference electrode (saturated KCl, 0.198 V vs. SHE) was placed near the outlet to separate the anode and cathode performance. To obtain reliable and reproducible results, at least 3 tests were conducted on two distinct cells. The electrochemical behavior was studied by electrochemical impedance spectroscopy (EIS) with cathode as the working electrode. Nyquist plots were recorded at OCV and perturbation amplitude of 10 mV was applied over the frequency range from 50 kHz to 0.5 Hz.

3. Results and discussions

3.1. Co-laminar flow visualization

The co-laminar flow inside the fuel cell at 10 and 5 mL h⁻¹ is shown in Fig. 2. Obviously, the two streams flow in parallel and no

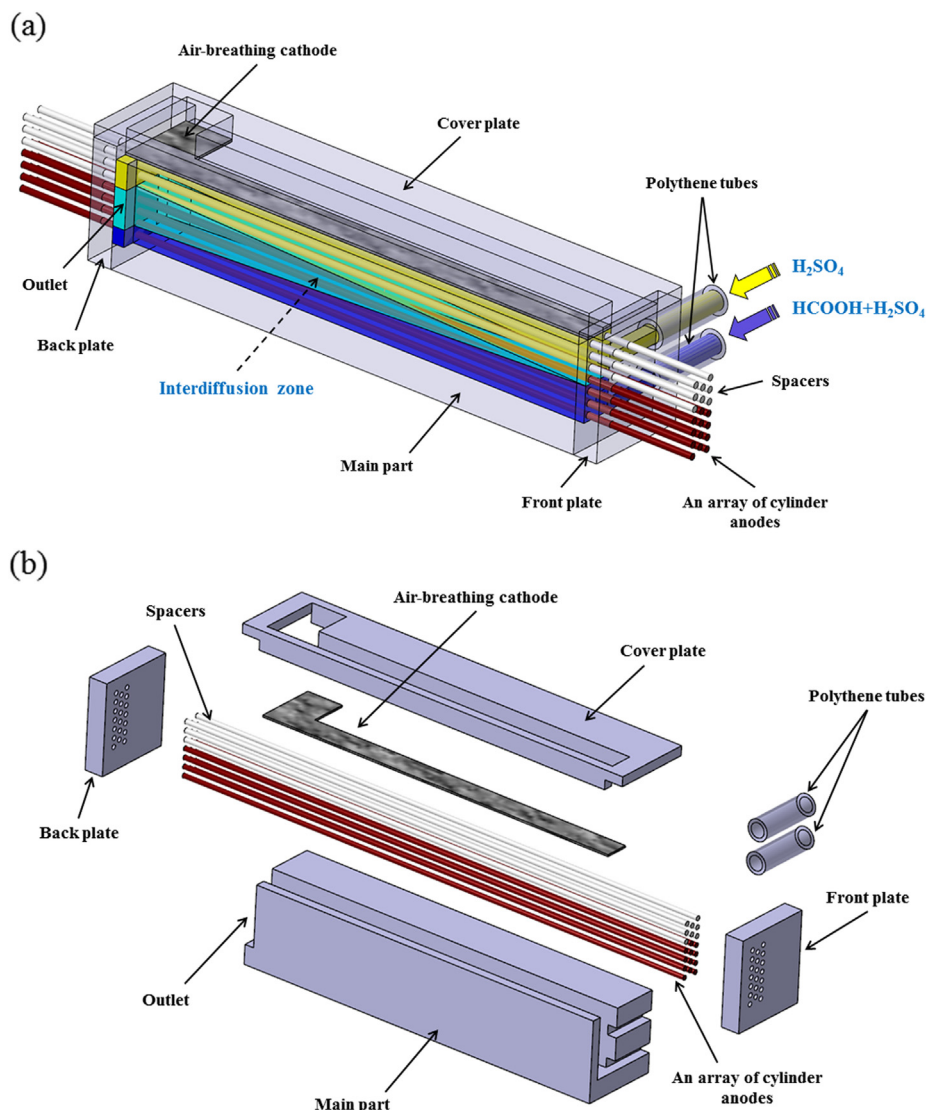


Fig. 1. Schematic illustration of (a) the air-breathing MMFC incorporating an array of cylinder anodes and (b) the detailed structure.

convective mixing is observed. A tapered interdiffusion zone forms from the beginning of the channel as a result of the transverse diffusion of red dye to the cathode side. At the channel end, the width of the interdiffusion zone is estimated to be 1.3 mm at

10 mL h^{-1} and 1.8 mm at 5 mL h^{-1} , respectively. This difference arises from the longer hydraulic retention time at the lower flow rate. In addition, Fig. 2 also suggests that all the volumetrically stacked cylinder anodes are immersed in the fuel stream and the



Fig. 2. Images of the co-laminar flow captured at 10 and 5 mL h^{-1} . Red dyed and dye-free deionized water were served as the anolyte and the electrolyte, respectively. (For interpretation of the references to color in this figure legend, the reader is referred to the web version of this article.)

interdiffusion zone, ensuring maximum utilization of the anode active sites and the fuel reactant.

3.2. Effect of the spacer configuration

Fig. 3 compares the performance of the MMFCs with 6 and 8 spacers. It's important to mention that this test was performed in the identical cell, but the two spacers adjacent to the cathode surface were removed for the test with 6 spacers. As shown in Fig. 3a, the performance of the MMFC with 8 spacers is quite low. On the contrary, the absence of the two spacers significantly improves the cell performance. The maximum current density raises up to 109.2 mA cm^{-2} and the peak power density is 19.1 mW cm^{-2} , 1.4 and 1.2 times higher than the former values, respectively. The cathode potential curve (Fig. 3b) further indicates that reactant transfer limitation occurs on the cathode for the cell with 8 spacers, but disappears after spacers removal. Such a distinct phenomenon implies that the spacer configuration greatly affects the cathodic reactant transfer.

On the air-breathing cathode, the consumption of protons and the generation of water contribute to the formation of a proton depletion boundary layer [33]. Meanwhile, the oxygen concentration in the catalyst layer can be considered as constant during

polarization [7,18]. Thus, the proton transport through the depletion boundary layer is the main factor differences the cathode performance. For the MMFC with 8 spacers, the distance between the cathode and the adjacent two spacers is only half of the minimum interspace between the rods, which can induce relatively large flow resistance and therefore decrease the local electrolyte velocity. As a result, both the convective proton transport and the replenishment to the proton depletion zone become sluggish, resulting in a large proton transfer resistance and then limiting the cell performance.

To validate this mechanism, EIS spectrum of the identical MMFC with 8 or 6 spacers are compared in Fig. 4. Obviously, the two Nyquist plots exhibit similar features and the most noticeable difference is the slope of straight lines at low frequencies. The slope of the fuel cell with 6 spacers is much lower than that of the cell with 8 spacers. As studied by Wang et al. [34], this slope is inversely proportional to the diffusion rate and can serve as a qualitatively empirical parameter to estimate the diffusion resistance. Hence, Fig. 4 demonstrates that the cathodic proton transfer resistance is reduced by removing the two spacers, confirming the mechanism discussed above. Also from Fig. 4, the total ohmic resistance of the cell with 6 spacers is estimated to be $13.4 \Omega \text{ cm}^{-2}$, lower than the cell with 8 spacers ($15.2 \Omega \text{ cm}^{-2}$). This total ohmic resistance comprises the contact resistance at the wire/electrode interface, the electric resistance of electrodes and the proton transfer resistance between the anode and cathode. Since the contact resistance and electrical resistance are constant in the identical cell, the decrease of total ohmic resistance is mainly caused by the reduced proton transfer resistance.

However, although both the proton transfer and cell performance can be enhanced by removing the two spacers, it's found that absence of more spacers would lead to flow instabilities (i.e., increased mixing and fuel crossover, data not shown). Consequently, the following experiments were all based on the fuel cell with 6 spacers.

3.3. Dynamic behavior of CO_2 bubbles

The dynamic behavior of CO_2 bubbles is shown in Fig. 5. As can be seen in these figures, the CO_2 bubbles nucleate on the anodes at downstream region ($t = 7 \text{ s}$) and adhere to the electrode forced by

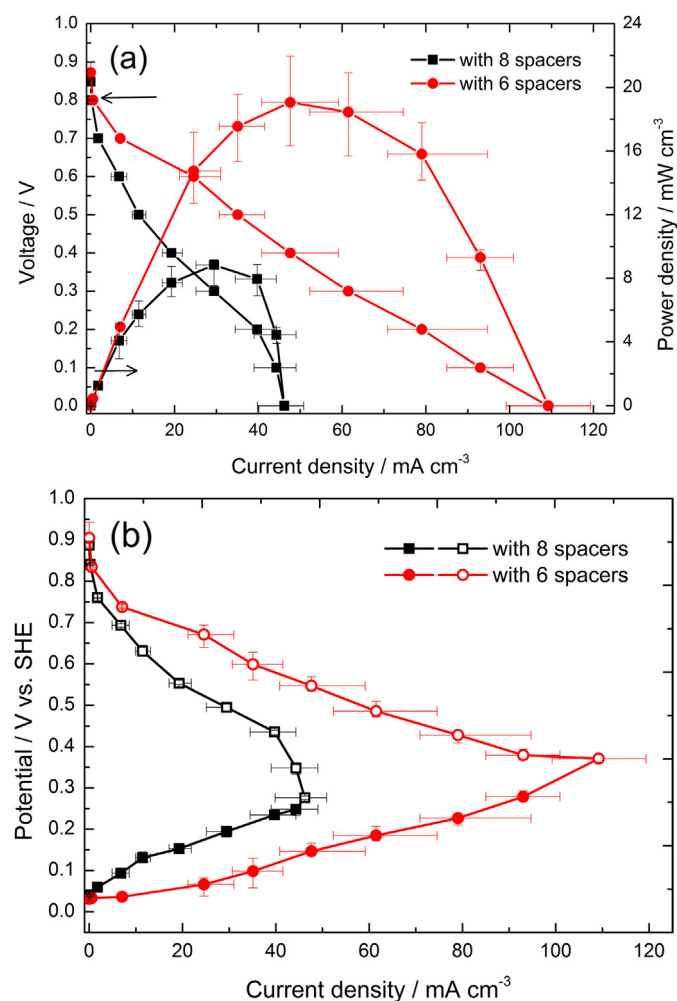


Fig. 3. Effect of the spacer configuration on the (a) cell performance and (b) electrode potentials at 20 mL h^{-1} . The fuel was $0.5 \text{ M HCOOH} + 0.5 \text{ M H}_2\text{SO}_4$ and the electrolyte was $0.5 \text{ M H}_2\text{SO}_4$.

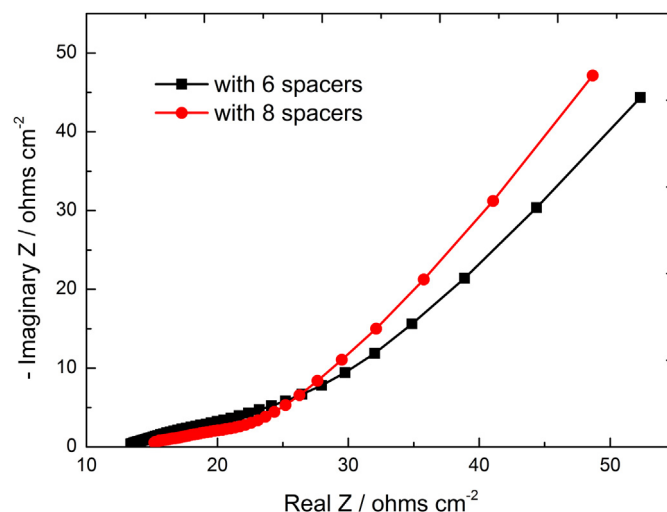


Fig. 4. Nyquist plots of the EIS measurements for the fuel cell with 6 or 8 spacers at 20 mL h^{-1} . The fuel was $0.5 \text{ M HCOOH} + 0.5 \text{ M H}_2\text{SO}_4$ and the electrolyte was $0.5 \text{ M H}_2\text{SO}_4$.

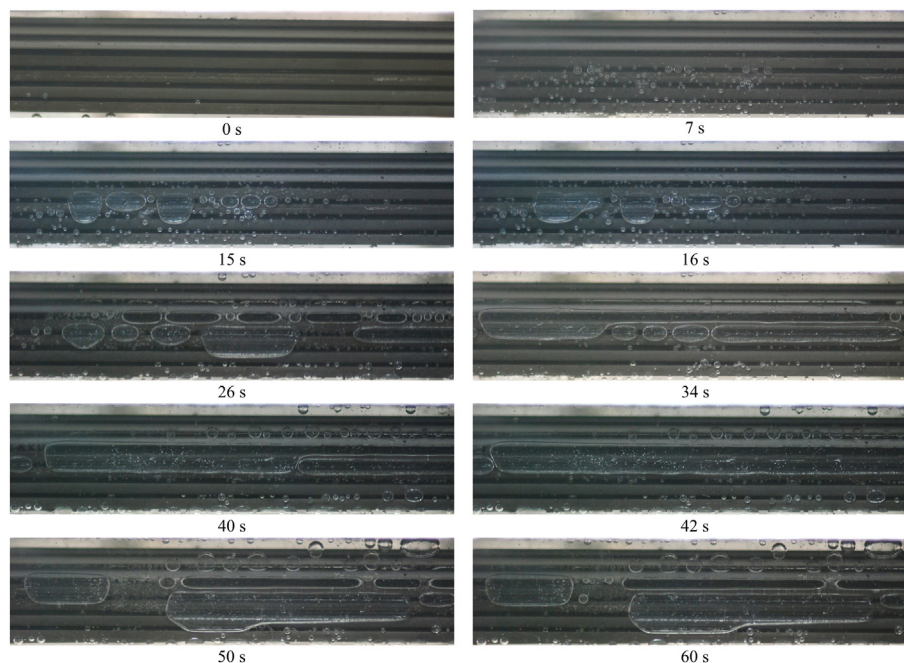


Fig. 5. Time evolution images of CO₂ gas bubbles in the presented MMFC. The fuel was 0.5 M HCOOH + 0.5 M H₂SO₄ and the electrolyte was 0.5 M H₂SO₄. The fluid flow was from right to left at 20 mL h⁻¹.

surface tension at the beginning of discharging. After 15–16 s of operation, these bubbles begin to coalesce into larger bubbles at the downstream part of the channel. This is reasonable as the fuel solution is more apt to be CO₂-saturated at the downstream. Once reach a certain size (approximately the rod spacing), the bubbles elongate along the anodes and form discontinuous gas slugs ($t = 26$ s). Interestingly, these slugs are constrained within the anodes array due to the surface tension of the gas/liquid interface and the confinement of the hexagon-arranged rods. Consequently, few gas bubbles are observed at the cathode side. This observation indicates that the perturbation effect of CO₂ bubbles on the colaminar interface is minimized, resulting in a stabilized electrolyte stream that prevents the fuel from reaching the cathode. However, as the constrained discontinuous slugs increase during the operation, fuel supply to the catalyst layer can be hindered ($t = 34, 40$ s). At 42 s, most of the inner volume is covered by the CO₂ slugs. Eventually, as the shear stress and the hydraulic pressure difference of the fluid overtakes the surface tension, the large CO₂ gas column is swept out by the flowing aqueous solution, exposing fresh anode surface area for further reaction. The scenario of CO₂ bubbles movement is repeated from $t = 50$ s on but in a shorter period. This distinct phenomenon suggests that the proposed MMFC is capable of handling the bubble distribution and removal. Furthermore, this unique bubble movement shows promising potential for passive fuel supply, as the fuel stream can be delivered by the removal of the CO₂ bubbles as in many self-refueling passive direct liquid fuel cells [35–37].

Meanwhile, the chronoamperometry curve of the MMFC during the visualization study is recorded and shown in Fig. 6. It is clear that the current density of the MMFC gradually decreases in the first 42 s. This phenomenon is mainly governed by the gradually increased coverage of the anode surface area and blockage of the convective fuel supply as a result of the emergence and coalescence of CO₂ bubbles (c.f. Fig. 5 and 0–42 s). After 42 s of operation, the current density of the MMFC undergoes substantial periodic fluctuations due to the periodic evolutions and subsequent removal of bubble slugs.

3.4. Cell performance

The effect of formic acid concentration on the cell performance and electrode potentials is shown in Fig. 7. It is obvious in Fig. 7a that the cell performance improves with increasing the fuel concentration from 0.1 to 0.5 M and declines at higher concentrations. As shown in Fig. 7b, the anode potential shows decreased oxidation kinetics at the formic acid concentration of 0.1 M, mainly due to the dilute reactant on the anode surface. Meanwhile, it is interesting to note that the cathode potential even increases at high current densities. This phenomenon can be attributed to the slightly enhanced oxygen reduction reaction (ORR) kinetics as a result of the accumulated joule and reaction heat [38]. However, this effect diminishes at higher fuel concentrations, as the cathode performance is gradually affected by increased fuel crossover (Fig. 7b).

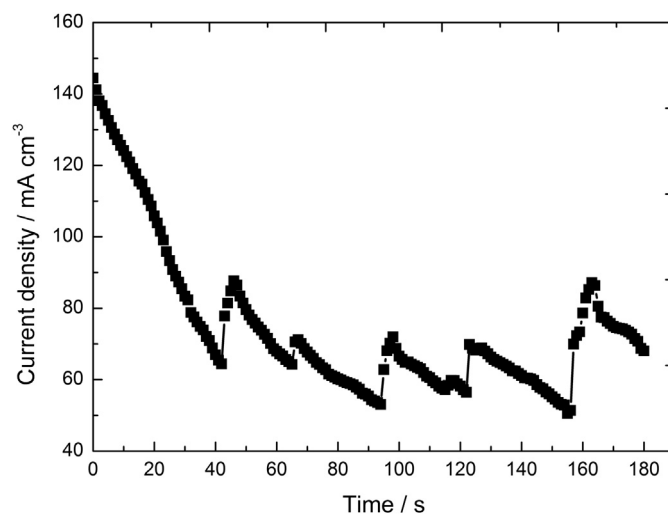


Fig. 6. The effect of CO₂ bubble movement on the corresponding chronoamperometry curve during the visualization study.

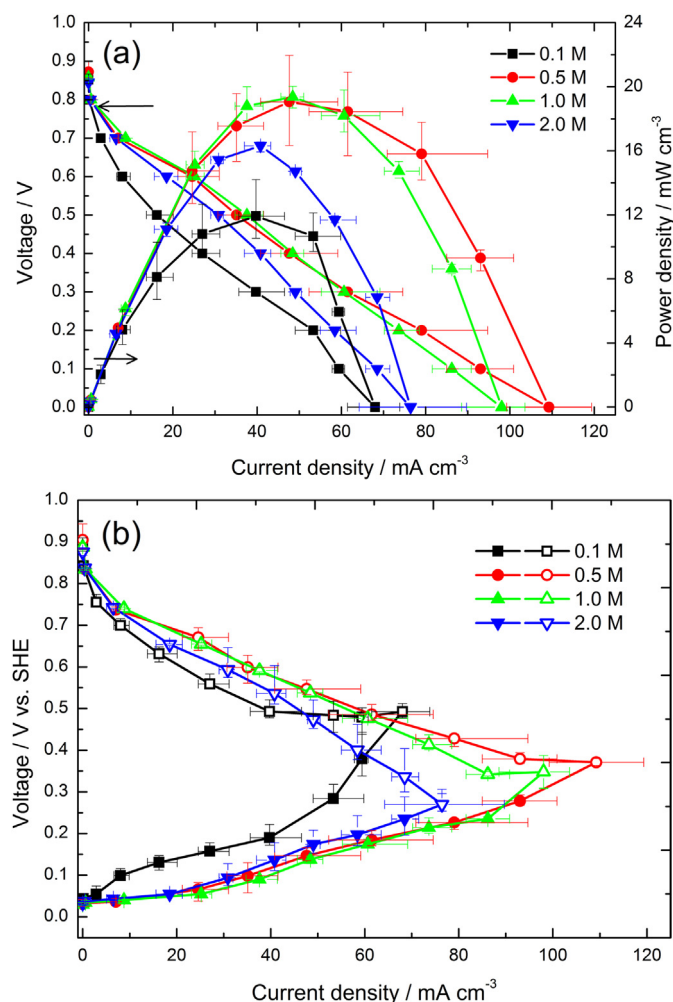


Fig. 7. Effect of formic acid concentration on the (a) cell performance and (b) electrode potentials. The electrolyte was 0.5 M H₂SO₄ and the flow rates were 20 mL h⁻¹.

Fig. 8a shows the effect of electrolyte concentration on the cell performance. As can be seen, the peak power density increases from 19.1 to 21.5 mW cm⁻³ upon increasing the electrolyte concentration from 0.5 to 1.0 M, mainly due to the reduced internal resistance [22,33] and enhanced ORR kinetics at higher electrolyte concentration (Fig. 8b). However, the cell performance declines when the electrolyte concentration rises up to 2.0 M. In this situation, the higher anode potential curve in Fig. 8b indicates that the anode suffers kinetic losses. This phenomenon can be attributed to the suppressed formic acid electro-oxidation resulting from the enhanced blockage of sulfate and bisulfate on the Pd catalyst active sites at higher H₂SO₄ concentration [33].

Fig. 9a shows the effect of flow rates on the cell performance. At the minimum flow rate of 1 mL h⁻¹, a relatively high OCV of 0.7 V and a peak power density of 4.8 mW cm⁻³ are obtained. This phenomenon can be attributed to the relatively high formic acid-tolerance of Pt catalyst in air-breathing MMFCs [39,40]. Hur et al. claimed that the HCOOH molecules desiring to oxidize on the Pt catalyst was ten orders of magnitude less than H⁺ ions ready to reduce the oxygen [40], therefore making the Pt catalyst seems to be formic acid-tolerant. As shown in Fig. 9a, the cell performance is significantly improved by increasing the flow rate from 10 to 20 mL h⁻¹. This is mainly due to the reduced fuel crossover and the enhanced convective reactant transfer. Furthermore, high flow rate also enhances the CO₂ bubble removal by increasing the shear

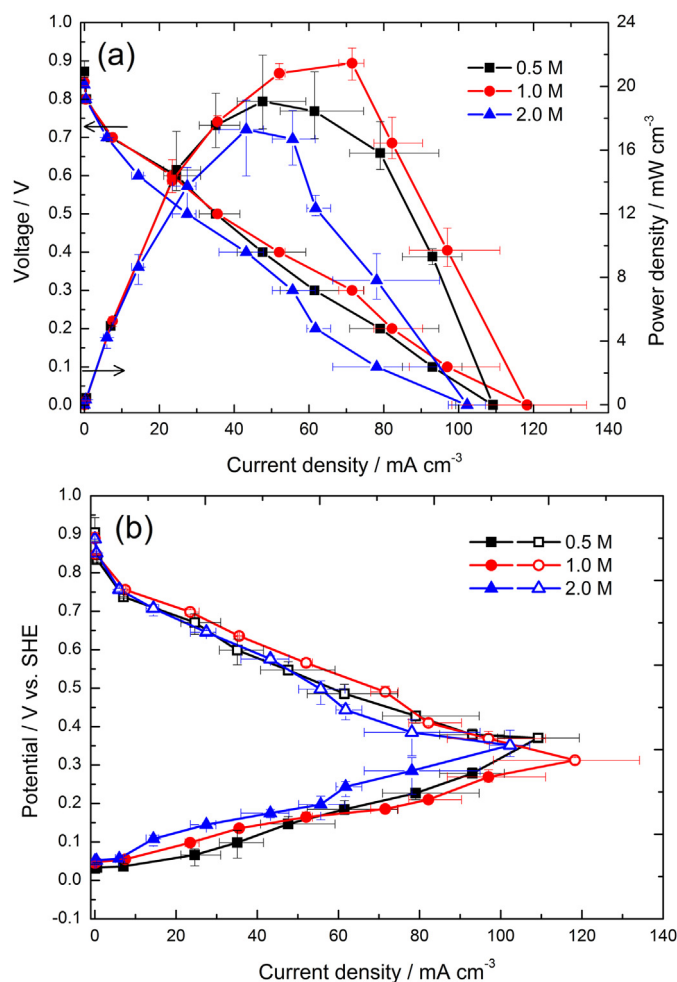


Fig. 8. Effect of electrolyte concentration on the (a) cell performance and (b) electrode potentials. The flow rates were 20 mL h⁻¹ and the formic acid concentration was 0.5 M.

stress and the hydraulic pressure difference. The presented MMFC yields the best performance at 20 mL h⁻¹, the limiting current density is 118.3 mA cm⁻³ and the peak power density is 21.5 mW cm⁻³. The maximum current output is 74.5 mA, comparable with that of the three-dimensional MMFC based on vanadium redox species [24]. However, the power output is lower (13.5 mW in this study and 28.0 mW in Ref. [24]), mainly due to the lower open circuit voltage (0.9 V vs. 1.2 V). The cell performance begins to decline at 30 mL h⁻¹. More obvious deviation from the optimum condition is observed at 60 mL h⁻¹, as a result of the fuel crossover caused by hydrodynamic instability [15].

As can be seen in Fig. 9b, the cathode performance is more significantly affected by the flow rate than the anode. For flow rates lower than 20 mL h⁻¹, the cathode performance gradually improves with the increase of flow rates due to the reduced fuel crossover effect. However, mixed potential can be induced at high flow rates (>30 mL h⁻¹) by the hydrodynamic instability [12,15,41], which makes the fuel stream touch the cathode on occasion and leads to severe fuel crossover. On the contrary, the anode performance is roughly steady for the flow rates spanning from 1 to 60 mL h⁻¹, indicating the harmful effect of the anodic depletion boundary layer has been mitigated. As the fuel stream is driven to flow through the anodes array, the depleted solution on the anode surface can be washed away by the fuel stream flowing around the cylinder anodes. Consequently, the local depleted zone can be

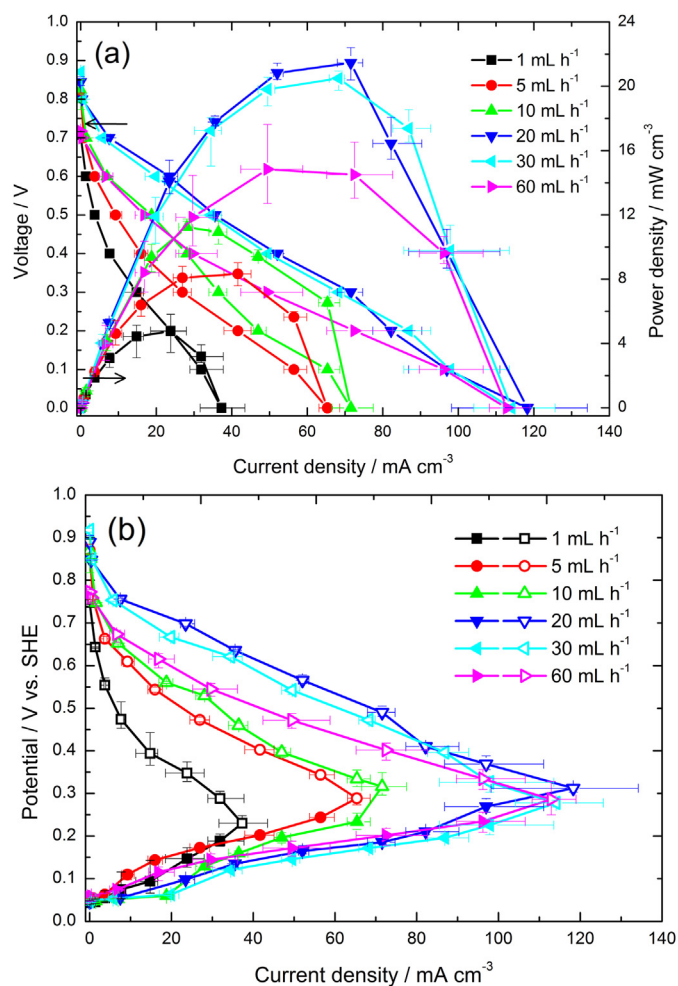


Fig. 9. Effect of reactant flow rates on the (a) cell performance and (b) electrode potentials. The fuel was 0.5 M HCOOH + 1 M H₂SO₄ and the electrolyte was 1 M H₂SO₄.

convectively replenished, enhancing the fuel transfer to the anode active sites.

Fig. 10 presents the single pass fuel utilization rates of the presented MMFC. The fuel utilization rate η is calculated by the following equation,

$$\eta = j / (nFC_0Q)$$

where j represents the maximum current output, n the released electrons per formic acid molecule ($n = 2$), F the faraday constant (96,485 C mol⁻¹), C_0 the inlet fuel concentration ($C_0 = 0.5$ M), Q the flow rate of fuel stream. As can be seen in Fig. 10, the fuel utilization rate goes down with the increase of flow rates. A maximum fuel utilization rate of 87.6% is achieved at the flow rate of 1.0 mL h⁻¹. This is mainly due to the extended reactive surface area and the volumetrically stacked anodes in the fuel stream and the interdiffusion zone (c.f., Fig. 2), which enable maximum fuel utilization. Furthermore, the enhanced local fuel transfer also contributes to the improved fuel utilization as discussed above. It's worthy to mention that the maximum fuel utilization rate in this study is higher than that of the three-dimensional MMFC using vanadium redox species (78%) [24] and just a little lower than that in a flow-through configuration (~100%) [20]. Since the presented MMFC eliminates the fuel/oxidant interdiffusion issue for potential fuel recycle and is expected to suffer less parasitic loss for overcoming

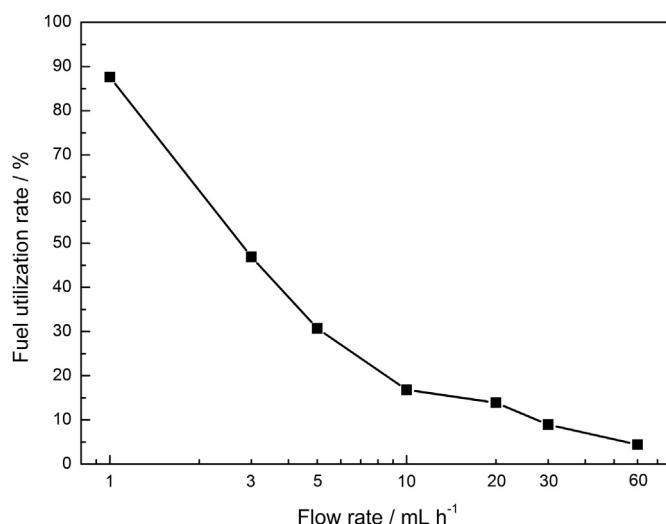


Fig. 10. Single pass fuel utilization rates under various flow rates. The fuel was 0.5 M HCOOH + 1.0 M H₂SO₄ and the electrolyte was 1.0 M H₂SO₄.

the pressure drop, it can be more applicable for high efficiency applications.

4. Conclusions

We proposed an air-breathing MMFC using graphite cylinder arrays as the anode in this study. The co-laminar fluid flow and dynamic behavior of CO₂ bubbles were visualized. The effects of spacer configuration, fuel and electrolyte concentration and reactant flow rate on the reactant transport and cell performance were investigated. Experimental results demonstrated that removal of the two spacers adjacent to the cathode surface significantly improved the cell performance by decreasing the proton transfer resistance. Most CO₂ bubbles can be constrained within the anodes array and would be expelled by the fluid flow periodically, therefore minimizing the perturbation to the electrolyte stream. However, the dynamic movement of bubbles can still affect the cell performance by covering the anode area and hindering the fuel supply. The presented fuel cell yielded a peak power density of 21.5 mW cm⁻³ and a maximum current density of 118.3 mA cm⁻³. The current output was 74.5 mA, comparable with the three-dimensional MMFC with vanadium redox species. A maximum fuel utilization rate up to 87.6% was obtained at the flow rate of 1 mL h⁻¹, mainly due to extended reactive surface area, enhanced mass transfer and the volumetrically stacked anodes configuration. The proposed microfluidic fuel cell provides a promising avenue for a high efficiency and even self-refueling MMFC.

Acknowledgments

The authors wish to thank the National Natural Science Foundation of China (Nos. 51006130, 51176212), New Century Excellent Talents in University (NCET-11-0551), Natural Science Foundation of Chongqing, China (No. cstcjjA90009) and National Natural Science Funds for Outstanding Young Scholar (No. 51222603) for the financial support to carry out this study.

References

- [1] E. Kjeang, N. Djilali, D. Sinton, J. Power Sources 186 (2009) 353–369.
- [2] S.A.M. Shaegh, N.T. Nguyen, S.H. Chan, Int. J. Hydrogen Energy 36 (2011) 5675–5694.

- [3] R.S. Jayashree, L. Gancs, E.R. Choban, A. Primak, D. Natarajan, L.J. Markoski, P.J.A. Kenis, *J. Am. Chem. Soc.* 127 (2005) 16758–16759.
- [4] R.S. Jayashree, D. Egas, J.S. Spendelow, D. Natarajan, L.J. Markoski, P.J.A. Kenis, *Electrochem. Solid-State Lett.* 9 (2006) A252.
- [5] S.A. Mousavi Shaegh, N.-T. Nguyen, S.H. Chan, *J. Power Sources* 209 (2012) 312–317.
- [6] S.A. Mousavi Shaegh, N.-T. Nguyen, S.H. Chan, W. Zhou, *Int. J. Hydrogen Energy* 37 (2012) 3466–3476.
- [7] S.A.M. Shaegh, N. Nam-Trung, C. Siew Hwa, *J. Micromech. Microeng.* 20 (2010) 105008.
- [8] D.T. Whipple, R.S. Jayashree, D. Egas, N. Alonso-Vante, P.J.A. Kenis, *Electrochim. Acta* 54 (2009) 4384–4388.
- [9] R.S. Jayashree, S.K. Yoon, F.R. Brushett, P.O. Lopez-Montesinos, D. Natarajan, L.J. Markoski, P.J.A. Kenis, *J. Power Sources* 195 (2010) 3569–3578.
- [10] S.K. Yoon, G.W. Fichtl, P.J.A. Kenis, *Lab. Chip* 6 (2006) 1516–1524.
- [11] A. Hollinger, R. Maloney, R.S. Jayashree, D. Natarajan, L.J. Markoski, P.J.A. Kenis, *J. Power Sources* 195 (2010) 3523–3528.
- [12] E.R. Choban, L.J. Markoski, A. Wieckowski, P.J.A. Kenis, *J. Power Sources* 128 (2004) 54–60.
- [13] R.F. Ismagilov, A.D. Stroock, P.J.A. Kenis, G. Whitesides, H.A. Stone, *Appl. Phys. Lett.* 76 (2000) 2376.
- [14] M.-H. Chang, F. Chen, N.-S. Fang, *J. Power Sources* 159 (2006) 810–816.
- [15] J.L. Cohen, D.A. Westly, A. Pechenik, H.D. Abruna, *J. Power Sources* 139 (2005) 96–105.
- [16] M. Sun, G. Velve Casquillas, S. Guo, J. Shi, H. Ji, Q. Ouyang, Y. Chen, *Microelectron. Eng.* 84 (2007) 1182–1185.
- [17] N.D. Mota, D.A. Finkelstein, J.D. Kirtland, C.A. Rodriguez, A.D. Stroock, H.D. Abruna, *J. Am. Chem. Soc.* 134 (2012) 6076–6079.
- [18] J. Xuan, D.Y.C. Leung, M.K.H. Leung, H. Wang, M. Ni, *J. Power Sources* 196 (2011) 9391–9397.
- [19] E. Kjeang, R. Michel, D.A. Harrington, N. Djilali, D. Sinton, *J. Am. Chem. Soc.* 130 (2008) 4000–4006.
- [20] E. Kjeang, R. Michel, D.A. Harrington, D. Sinton, N. Djilali, *Electrochim. Acta* 54 (2008) 698–705.
- [21] D. Krishnamurthy, E.O. Johansson, J.W. Lee, E. Kjeang, *J. Power Sources* 196 (2011) 10019–10031.
- [22] K.S. Salloum, J.R. Hayes, C.A. Friesen, J.D. Posner, *J. Power Sources* 180 (2008) 243–252.
- [23] J.W. Lee, E. Kjeang, *Int. J. Hydrogen Energy* 37 (2012) 9359–9367.
- [24] E. Kjeang, J. McKechnie, D. Sinton, N. Djilali, *J. Power Sources* 168 (2007) 379–390.
- [25] W.R. Merida, G. McLean, N. Djilali, *J. Power Sources* 102 (2001) 178–185.
- [26] B. Zhang, D. Ye, J. Li, X. Zhu, Q. Liao, *J. Power Sources* 214 (2012) 277–284.
- [27] E. Kjeang, A.G. Brolo, D.A. Harrington, N. Djilali, D. Sinton, *J. Electrochem. Soc.* 154 (2007) B1220.
- [28] S. Hasegawa, K. Shimotani, K. Kishi, H. Watanabe, *Electrochem. Solid State Lett.* 8 (2005) A119–A121.
- [29] A. Li, S.H. Chan, N.T. Nguyen, *J. Micromech. Microeng.* 17 (2007) 1107.
- [30] J.-C. Shyu, C.-L. Huang, *J. Power Sources* 196 (2011) 3233–3238.
- [31] J.-C. Shyu, C.-S. Wei, C.-J. Lee, C.-C. Wang, *Appl. Therm. Eng.* 30 (2010) 1863–1871.
- [32] J. Li, D.-d. Ye, X. Zhu, Q. Liao, Y.-d. Ding, X. Tian, *J. Appl. Electrochem.* 39 (2009) 1771–1778.
- [33] R.S. Jayashree, M. Mitchell, D. Natarajan, L.J. Markoski, P.J.A. Kenis, *Langmuir* 23 (2007) 6871–6874.
- [34] X.Y. Wang, J. Yan, H.T. Yuan, Y.S. Zhang, D.Y. Song, *Int. J. Hydrogen Energy* 24 (1999) 973–980.
- [35] N. Paust, S. Krumbholz, S. Munt, C. Müller, P. Koltay, R. Zengerle, C. Ziegler, *J. Power Sources* 192 (2009) 442–450.
- [36] N. Paust, C. Litterst, T. Metz, M. Eck, C. Ziegler, R. Zengerle, P. Koltay, *Microfluid. Nanofluid.* 7 (2009) 531–543.
- [37] C. Litterst, S. Eccarius, C. Hebling, R. Zengerle, P. Koltay, *J. Micromech. Microeng.* 16 (2006) S248–S253.
- [38] Y.H. Pan, *J. Power Sources* 161 (2006) 282–289.
- [39] J. Hur, D. Meng, C.J. Kim, in: *IEEE Int. Conf. MEMS*, pp. 168–171, Hong Kong, China, Jan. 2010.
- [40] J. Hur, D. Meng, C.J. Kim, *J. Microelectromech. Syst.* 12 (2012) 476–483.
- [41] P.O. López-Montesinos, N. Yossakda, A. Schmidt, F.R. Brushett, W.E. Pelton, P.J.A. Kenis, *J. Power Sources* 196 (2011) 4638–4645.